Received 16 March 2018; revised 4 May 2018; accepted 5 May 2018. Date of publication 15 May 2018;
date of current version 8 June 2018. The review of this paper was arranged by Editor M. Chan.

Digital Object Identifier 10.1109/JEDS.2018.2834825

Band-Tails Tunneling Resolving the Theory-Experiment Discrepancy in Esaki Diodes

JASPER BIZINDAVYI [1,2], ANNE S. VERHULST [2], QUENTIN SMETS [2], DEVIN VERRECK [2], BART SORÉE [1,2,3] (Member, IEEE), AND GUIDO GROESENEKEN [1,2] (Fellow, IEEE)

1 Department of Electrical Engineering, KU Leuven, 3001 Leuven, Belgium
2 imec, 3001 Leuven, Belgium
3 Department of Physics, Universiteit Antwerpen, 2020 Antwerp, Belgium

CORRESPONDING AUTHOR: J. BIZINDAVYI (e-mail: jasper.bizindavyi@imec.be)

This work was supported by imec's Industrial Affiliation Program.

ABSTRACT Discrepancies exist between the theoretically predicted and experimentally measured performance of band-to-band tunneling devices, such as Esaki diodes and tunnel field-effect transistors (TFETs). We resolve this discrepancy for highly-doped, direct-bandgap Esaki diodes by successfully calibrating a semi-classical model for high-doping-induced ballistic band-tails tunneling currents at multiple temperatures with two $In_{0.53}Ga_{0.47}As$ Esaki diodes using their SIMS doping profiles, C-V characteristics and their forward-bias current density in the negative differential resistance (NDR) regime. The current swing in the NDR regime is shown not to be linked to the band-tails Urbach energy. We further demonstrate theoretically that the calibrated band-tails contribution is also the dominant band-tails contribution to the subthreshold swing of the corresponding TFETs. Lastly, we verify that the presented procedure is applicable to all direct-bandgap semiconductors by successfully applying it to InAs Esaki diodes in literature.

INDEX TERMS Band-tails, high-doping effect, Esaki diode, density-of-states, negative differential resistance, TFET, III-V semiconductors.

I. INTRODUCTION

The needs of future ultra-low power applications have fueled the quest for novel power efficient devices such as the tunnel field-effect transistor (TFET) [1], [2]. The TFET's potential for a sub-60 mV/dec subthreshold swing (SS) arises from its use of quantum mechanical (QM) band-to-band tunneling (BTBT) to inject charge carriers into the channel [3]–[6]. To bridge the existing gap between simulation predictions for ideal TFETs and the lagging experimental results of fabricated devices, significant efforts are being made to develop models for some of the main causes of suboptimal performance, such as trap-assisted tunneling (TAT) [7], [8], phonon-assisted tunneling (PAT) [9], and Auger generated leakage currents [10]. For high-doping-induced band-tails tunneling currents, there are some purely predictive studies [11]–[13], qualitative analyses [14], and a recent work in which an effort is made to extract the band edge decay parameter (Urbach energy) using a simple model [15]. However, no attempts have been made at a full current calibration nor at a quantitative extraction of the band-tails density-of-states (DOS) using electrical measurements. The latter is typically extracted using optical measurement techniques [16]–[18], which limits its use towards predicting its electrical performance impact. Nevertheless, to achieve a high on-current in TFETs, high doping concentrations are required and, therefore, band-tails will be present.

In this work, we therefore report on the successful calibration of a semi-classical (SC) model for high-doping-induced ballistic band-tails tunneling using the experimental I-V data of two $In_{0.53}Ga_{0.47}As$ *p-i-n* Esaki diodes at multiple temperatures. We show that the band-tails model can be used to extract the band-tails DOS and we determine the physical meaning behind the band-tails signature in the

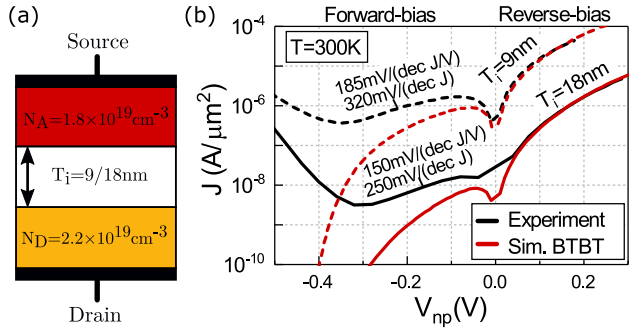

FIGURE 1. **(a) Schematic structure and (b) measured current-voltage characteristics (black) of the $In_{0.53}Ga_{0.47}As$ *p-i-n* Esaki diodes. (b) The simulated BTBT current densities (red) provide the best match in reverse-bias (parameters in Table 2). For $T_i = 9$ nm: $\Delta x_{shift} = 9$ nm, as detailed in the body text.**

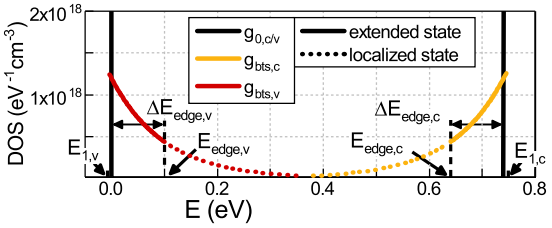

FIGURE 2. **The conduction (gold) and valence (red) band-tails DOS, Eq. (2). The unperturbed conduction and valence band DOS are also shown (black).**

forward-bias current density. Further, it is verified that the calibration of Esaki diodes is relevant for exploring the performance of the corresponding TFET. Lastly, the full procedure is employed to explain the measured current-voltage characteristics of two highly-doped InAs Esaki diodes [19], demonstrating the procedure's applicability to all direct-bandgap semiconductors.

II. STRUCTURE AND I-V CHARACTERISTICS OF THE $IN_{0.53}GA_{0.47}AS$ ESAKI DIODES

The disparity between the theoretical models and the experimental results is observable in the $In_{0.53}Ga_{0.47}As$ *p-i-n* Esaki diodes whose schematic structure and current-voltage characteristics are shown in Fig. 1. The $In_{0.53}Ga_{0.47}As$ Esaki diodes have been grown epitaxially on lattice-matched InP(001) substrates using molecular beam epitaxy (additional fabrication details are provided in [20]). The diodes have an intrinsic region thickness of about 9 and 18 nm, a *n*-type silicon doping concentration of 2.2×10^{19} cm^{-3} and a *p*-type beryllium doping concentration of 1.8×10^{19} cm^{-3}, see Fig. 1(a). The SIMS measurements for the 18 nm Esaki diode show that the doping profiles decay with 6 nm/dec [20]. The diodes have been used in a previous study for the calibration of SC and QM BTBT models [20]. Despite the good match in reverse-bias (Fig. 1(b)), there remains a significant mismatch between the measured currents and the simulated BTBT currents (calculated using the dynamic nonlocal SC BTBT model in Sentaurus Device [21]) in the forward-bias negative differential resistance (NDR) regime of both diodes. The current density in the NDR regime cannot be purely BTBT. This conclusion results from an in-depth study, [22], in which an attempt has been made to match the experimental data using only BTBT current, based on the recalibration of the effective conduction/valence band tunneling mass $m_{c/v}$, the Fermi level position (through the electron and heavy hole effective mass, resp. $m_{e,\Gamma}$ and m_{hh}) and the Jain-Roulston parameters [23] for dopant-dependent bandgap narrowing (which can be best understood as a quasi-rigid shift of the bulk conduction and valence band because of high-doping-induced many-body interactions [24]). This attempt at matching has been unsuccessful, as it required unphysical values for the model parameters [22]. Similarly, Cho *et al.* concluded that their bandgap-narrowing-inclusive ballistic NEGF approach could not completely explain the forward-bias mismatch [25]. Moreover, trap-assisted tunneling (TAT) because of bulk traps cannot explain the discrepancy either, since straightforward SC TAT models predict TAT current contributions which increase with the forward-bias voltage [26]. In this work, we therefore posit and verify the hypothesis that the forward-bias mismatch originates from ballistic tunneling current contributions because of high-doping-induced band-tails states.

III. SEMI-CLASSICAL BAND-TAILS MODEL

Band-tails in the bandgap of a material arise from sources of structural or thermal disorder [13]. In the case of highly-doped semiconductor materials, the physical origin of band-tails states is mainly attributed to the random spatial fluctuations of the dopant atoms [24], [27], which is what we focus on in this work. As described in [28], our model accounts for band-tails states by employing an approach similar to that of Khayer and Lake in [12], but now in a SC framework. More specifically, an artificial band-tails state energy dispersion relation $E_{bts,c/v}(k)$ is assumed, where E_{bts} is the band-tails state energy and k the corresponding wave vector magnitude:

$$k = k_{1,c/v}\exp\left(\pm\frac{E_{bts} - E_{1,c/v}}{3E_{0,c/v}}\right) \text{ for: } \begin{cases} E_{bts} < E_{1,c} \\ E_{bts} > E_{1,v}, \end{cases} \quad (1)$$

where $+(-)$ refers to the conduction(valence) band-tails, $E_{1,c/v}$ and $k_{1,c/v}$ specify the starting point of the band-tails, and $E_{0,c/v}$ is the Urbach energy. From these spherically symmetric dispersion relations, expressions for the band-tails DOS $g_{bts,c/v}$ are found which correctly reproduce the exponential decrease with energy as reported by both theoretical [29] and experimental works [16] (Fig. 2):

$$g_{bts,c/v}(E_{bts}) = \frac{k_{1,c/v}^3}{3\pi^2 E_{0,c/v}}\exp\left(\pm\frac{E_{bts} - E_{1,c/v}}{E_{0,c/v}}\right). \quad (2)$$

Note that neither the dispersion relation nor the band-tails DOS explicitly depend on the concentration, the type, or the activation energy of the dopant atom, since the interdependence is poorly understood and has not yet been detailed in

TABLE 1. The left and right boundary voltages, for the experimental data of Fig. 1(b), used during the calibration.

T_i=18 nm	V_{fwd}	V_{rev}	T_i=9 nm	V_{fwd}	V_{rev}
300 K	−0.52 V	0.185 V	298 K	−0.53 V	0.02 V
77 K	−0.64 V	0.175 V	78 K	−0.73 V	0.045 V

literature. In addition, note that Eq. (1) implicitly assumes a one-to-one correspondence between energy and wave vector for the band-tails states, which is only the case for completely delocalized states such as bulk band states. However, this is an acceptable approximation for band-tails states within a small range ($\sim$ 100 meV) from the unperturbed band edges, since they can be considered to be spatially extended states [30], [31]. In our model, we further assume an abrupt transition from these delocalized to strongly localized band-tails states at an energy $\Delta E_{\mathrm{edge,c/v}}$ from the unperturbed band edges (Fig. 2). The current contributions, arising from tunneling transitions between delocalized conduction and valence band-tails states, $J_{\mathrm{bts}\leftrightarrow\mathrm{bts}}$, bulk valence and conduction band-tails states, $J_{\mathrm{v}\leftrightarrow\mathrm{c,bts}}$, and bulk conduction and valence band-tails states, $J_{\mathrm{c}\leftrightarrow\mathrm{v,bts}}$, are calculated similarly to BTBT using the Tsu-Esaki expression [32] (where polar coordinates are used for the orthogonal wave vector components):

$$J_{\substack{\mathrm{bts}\leftrightarrow\mathrm{bts}\\ \mathrm{v}\leftrightarrow\mathrm{c,bts}\\ \mathrm{c}\leftrightarrow\mathrm{v,bts}}} = \frac{q}{2\pi^2\hbar}\int_{x_\mathrm{l}}^{x_\mathrm{r}} q\vec{E}(x)\int_{\forall k_\perp} k_\perp T(E_{\substack{\mathrm{bts,v}\\ \mathrm{v}}}(x),k_\perp) \times\left[f_\mathrm{n}(E_{\substack{\mathrm{bts,c}\\ \mathrm{c}}}(x',k_\perp)) - f_\mathrm{p}(E_{\substack{\mathrm{bts,v}\\ \mathrm{v}}}(x,k_\perp))\right]\mathrm{d}k_\perp\mathrm{d}x \tag{3}$$

with $\vec{E}$ the local electric field, $x_{\mathrm{l/r}}$ the left/right contact position, T the transmission probability, and $x' = x + l_{\mathrm{tun}}$ [28]. In Eq. (3), tunneling transitions without a complete ballistic path between the left and right contact are excluded through the transmission probability: $T = T_{\mathrm{WKB}} \times T_\mathrm{L} \times T_\mathrm{R}$. T_{WKB} is the WKB tunneling probability (see [28]) and $T_{\mathrm{L(R)}}$ equals 1 if a ballistic path between the left(right) contact and the initial(final) state of the tunnel path exists and 0 otherwise (Fig. 3).

IV. CALIBRATION OF THE CONVENTIONAL BTBT MODEL

Before calibrating the band-tails model, the conventional BTBT current, calibrated for achieving the best simultaneous fit with the reverse-bias current density of both $In_{0.53}Ga_{0.47}As$ diodes, is shown in Fig. 1(b). A recalibration of the BTBT current, compared to [20], occurred since a prefactor of $\sqrt{m_{\mathrm{r,y}}}\sqrt{m_{\mathrm{r,z}}}/\sqrt{m_{\mathrm{r,x}}} = 1.67$ had to be added to the dynamic nonlocal BTBT model, because QM simulations show direct-bandgap materials to have an anisotropic reduced tunneling mass m_r [33]. In addition, the considered reverse-bias range has been limited to V_{rev} (Table 1), such that only data points unaffected by series resistance are

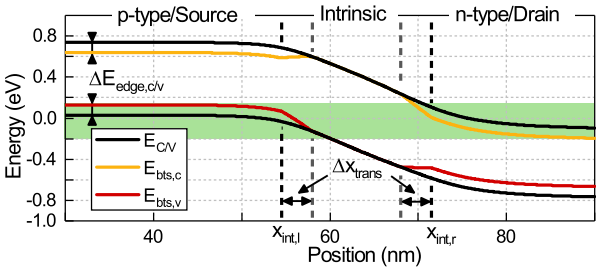

FIGURE 3. Band diagram around the tunnel junction of a T_i = 18 nm *p-i-n* Esaki diode for V_{np} = −0.30 V, showing the unperturbed bulk band edges (black) and the band-tails states for which $\Delta E_{\mathrm{edge,c/v}}$ = 100 meV. For ballistic transitions in the tunneling window (green shaded area): $T_L = T_R = 1$.

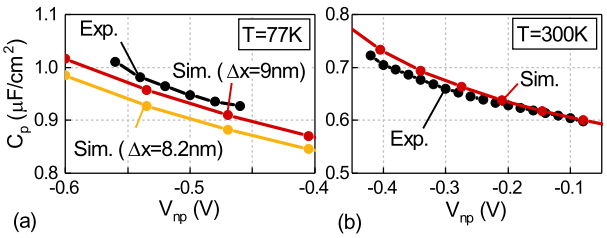

FIGURE 4. Comparison between the measured (black) and simulated (colored) capacitance-voltage characteristics for (a) the T_i = 9 nm and (b) the T_i = 18 nm $In_{0.53}Ga_{0.47}As$ *p-i-n* Esaki diodes. (a) The simulated capacitance curves were calculated using the SIMS doping profile of the T_i = 18 nm Esaki diode for which the Be-profile was shifted with $\Delta x_{\mathrm{shift}}$ = 9 nm (red) or 8.2 nm (gold), as detailed in the body text.

included. The calibration results for m_c, m_v, $m_{\mathrm{e},\Gamma}$, m_{hh} and the Jain-Roulston parameters are given in Table 2 and shown in Fig. 1(b). The large values for m_c and m_v might indicate that SC models overestimate the theoretically achievable tunneling probabilities [34]. During the calibration, the SIMS doping profiles of the T_i = 18 nm Esaki diode (profile set 2 of [20]) have been used for the T_i = 9 nm Esaki diode, after shifting the beryllium doping profile closer to the silicon profile with the (processing target) value of $\Delta x_{\mathrm{shift}}$ = 9 nm, as no SIMS profiles are available for this diode. This choice is based on the observation that two of the four Esaki diodes of [20] have the same average doping concentration and doping profile steepness. The only unknown parameter for the T_i = 9 nm diode is therefore the exact distance between the silicon and beryllium doping profile. Verification of the C-V characteristics using the calibrated parameters shows that the maximum relative difference between the simulated and measured total capacitance is small: 3%/3.5% for the T_i = 9 nm/18 nm diode (Fig. 4), which supports the correctness of the doping profiles and hence the calibration itself.

V. CALIBRATION OF THE BAND-TAILS TUNNELING MODEL

Next, the Urbach energy $E_{0,\mathrm{c/v}}$ and $k_{1,\mathrm{c/v}}$ parameters of the SC band-tails model have been calibrated using the current density in the NDR regime of both Esaki diodes (limited to

TABLE 2. Calibrated BTBT model parameters. $\{X_i\}_{n/p}$ are the Jain-Roulston parameters for n/p-type doped $In_{0.53}Ga_{0.47}As$.

Effective masses	Jain-Roulston bandgap narrowing parameters	
$m_c = 0.054$	$A_n = 1.3 \times 10^{-8}$ eVcm	$A_p = 5.4 \times 10^{-9}$ eVcm
$m_v = 0.065$	$B_n = 3.4 \times 10^{-7}$ eVcm$^{3/4}$	$B_p = 1.4 \times 10^{-7}$ eVcm$^{3/4}$
$m_{e,\Gamma} = 0.043$	$C_n = -2.3 \times 10^{-13}$ eVcm$^{3/2}$	$C_p = 1.9 \times 10^{-13}$ eVcm$^{3/2}$
$m_{hh} = 0.550$	$D_n = 2.5 \times 10^{-12}$ eVcm$^{3/2}$	$D_p = 1.4 \times 10^{-12}$ eVcm$^{3/2}$

TABLE 3. Calibrated band-tails model parameters for different $\Delta E_{edge,c/v}$. The ratio Λ, used to determine the position x_{int}, is defined as $\Lambda \triangleq N_{A(D)}(x = x_{int,l(r)})/N_{A(D)}(x = x_{l(r)})$. For all cases, $E_{1,c/v} = E_{c/v} \pm 5$ meV and $\Delta x_{trans} = 3.5$ nm.

$\Delta E_{edge,c/v}$	$E_{0,c/v}$	$k_{1,c/v}$	$\Lambda_{T_i=18\,nm}$	$\Lambda_{T_i=9\,nm}$
100 meV	100 meV	1.6×10^8 m^{-1}	35%	45%
70 meV	100 meV	2.6×10^8 m^{-1}	35...40%	45%
50 meV	100 meV	3.8×10^8 m^{-1}	35...40%	45%

V_{fwd}, see Table 1) with $E_{1,c/v} = E_{c/v} \pm 5$ meV. During the calibration, it has been assumed that at each position in the device: $E_{0,c} = E_{0,v}$ and $k_{1,c} = k_{1,v}$. It has been noted, however, that the contribution of band-tails states in the minority band to the tunneling current is negligible, both in forward-bias and reverse-bias, such that, in fact, it would have been sufficient to only define band-tails in the majority band (this is the valence band of the *p*-type doped material and the conduction band of the *n*-type doped material). In addition, we have assumed, as a first guess, that $\Delta E_{edge,c/v} = 100$ meV, which is based on theoretical calculations that deal with the transition from spatially localized to extended band-tails states in amorphous materials [30], [31], since no equivalent data is available for III-V semiconductor materials. The Esaki diodes of Fig. 1(a) are ideally suited to verify the band-tails model, since, on the one hand, the Esaki diodes have the same *n*-type and *p*-type doping profiles, which implies an identical band-tails content in the identically doped regions, while, on the other hand, the two diodes have a distinctly different I-V characteristic due to the difference in intrinsic region thickness, T_i. Because band-tails are only present in highly-doped regions, our model includes a transition region that extends from the interface, x_{int}, between a highly-doped and intrinsic region into the intrinsic region with a length of Δx_{trans} (Fig. 3). In this transition region, the density and energetic extension of the band-tails into the bandgap are reduced until they disappear. This is implemented by linearly increasing (decreasing) $E_{1,c(v)}$ in Eq. (1), which shifts the band-tails into the bulk bands. The interface, x_{int}, between a highly-doped and intrinsic region in the $T_i = 18/9$nm diode is defined as that position for which the majority doping concentration has decreased to $\Lambda_{T_i=18/9\,nm}$ percent (targeted to be around 50%, see Table 3) of its average level in the doped region. We also assume that the band-tails DOS decreases proportionally to the doping profiles, which decay with 6 nm/dec beyond x_{int} [20], resulting in $\Delta x_{trans} = 3.5$ nm. As a result, our model directly relates the band-tails DOS to the local doping concentration profiles through x_{int} and Δx_{trans}. In a more rigorous model, this would be done through the electron screening length, which affects the band-tails and is a function of the local impurity concentration [35], [36].

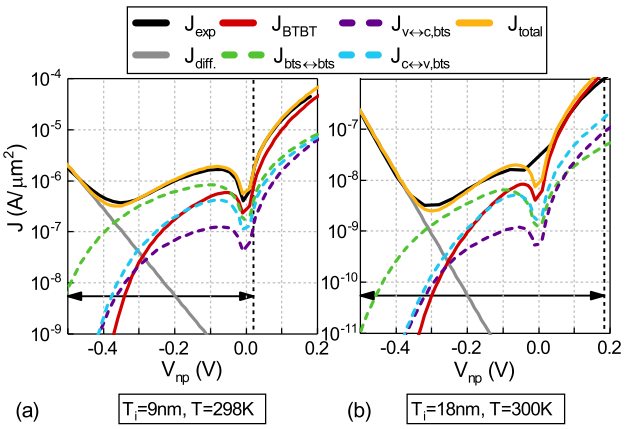

FIGURE 5. Result of the calibrated band-tails model for $\Delta E_{edge,c/v} = 100$ meV using the parameter values given in Table 3, for the (a) $T_i = 9$ nm ($\Delta x_{shift} = 8.2$ nm) and (b) $T_i = 18$ nm $In_{0.53}Ga_{0.47}As$ *p-i-n* Esaki diodes at T = 300 K. J_{BTBT} has been calculated using the parameters of Table 2. $J_{diff.}$ is an exponential fit to the SRH current. The arrows show the calibration range (Table 1).

The result of the calibration for $\Delta E_{edge,c/v} = 100$ meV is shown in Fig. 5(a) and Fig. 5(b) for, respectively, the $T_i = 9$ nm and $T_i = 18$ nm Esaki diode. In case of the $T_i = 9$ nm diode, the calibration includes a doping profile re-optimization to compensate for an observable band-tails contribution in reverse-bias. In particular, the doping profile shift is decreased to $\Delta x_{shift} = 8.2$ nm. The resulting maximum simulation-experiment capacitance difference remains small: 6% (Fig. 4), confirming that the used doping profile remains acceptable. The calibrated parameter values are given in Table 3 for band-tails and remain as in Table 2 for

TABLE 4. Calibrated values of $\rho_{2D,bts,20\%}$, the 2D band-tails DOS integrated over 20% of $\Delta E_{edge,c/v}$, for different values of $\Delta E_{edge,c/v}$ and $E_{0,c/v}$. The corresponding 3D band-tails DOS, averaged over the same energy interval, are also given.

$\Delta E_{edge,c/v}$	$E_{0,c/v}$	$\rho_{2D,bts,20\%}$	avg[$DOS_{3D,bts,20\%}$]
100 meV	30 meV	3.1×10^9 cm^{-2}	1.6×10^{17} eV^{-1} cm^{-3}
	70 meV	4.1×10^9 cm^{-2}	3.8×10^{17} eV^{-1} cm^{-3}
	100 meV	4.3×10^9 cm^{-2}	4.9×10^{17} eV^{-1} cm^{-3}
	150 meV	4.3×10^9 cm^{-2}	5.9×10^{17} eV^{-1} cm^{-3}
70 meV	100 meV	9.8×10^9 cm^{-2}	2.8×10^{18} eV^{-1} cm^{-3}
50 meV	100 meV	1.7×10^{10} cm^{-2}	1.1×10^{19} eV^{-1} cm^{-3}

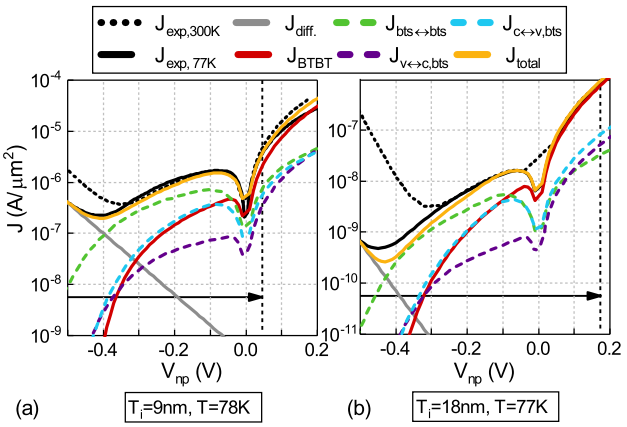

FIGURE 6. Low temperature verification: result of the band-tails model for $\Delta E_{edge,c/v} = 100$ meV using the parameter values given in Table 3, for the (a) $T_i = 9$ nm ($\Delta x_{shift} = 8.2$ nm) and (b) $T_i = 18$ nm $In_{0.53}Ga_{0.47}As$ diodes at T = 77 K. Other details: see Fig. 5.

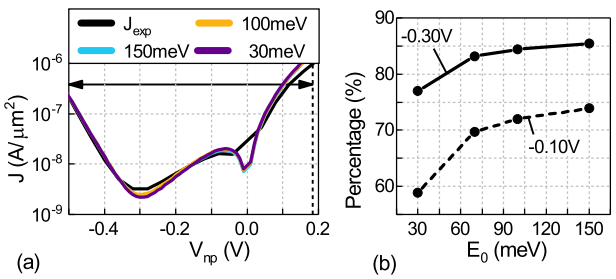

FIGURE 7. The signature of band-tails in the NDR regime is not linked to the Urbach energy, E_0, but to the deep tail of extended band-tails states: (a) Calibration results for different values of $E_{0,c/v}$ for the $T_i = 18$ nm Esaki diode at T = 300 K. $\Delta E_{edge,c/v} = 100$ meV. (b) Percentage of $J_{bts,total} = J_{bts\leftrightarrow bts} + J_{v\leftrightarrow c,bts} + J_{c\leftrightarrow v,bts}$ generated by the band-tails states in the first 20 meV from $E_{edge,c/v}$ for multiple V_{np} (Fig. 2).

BTBT. It is clear that a complete match over the entire calibration range (and beyond) is achieved for both diodes, when taking our calibrated ballistic band-tails tunneling contribution into account. This match for two different Esaki diodes is not a definitive proof that the measured current densities in the NDR regime are due to band-tails, though it makes it very likely. Strictly speaking, however, the band-tails DOS calibration results should be seen as an upper limit, since it might be possible that phonon-assisted tunneling [9] or thermal band-tails contribute an observable current as well.

When performing simulations at 77 K using the parameter set for $\Delta E_{edge,c/v} = 100$ meV, a good match between the simulated currents and the low temperature data of the Esaki diodes is maintained (Fig. 6), further supporting the correctness of the model. Note that the experimental data at 77 K are practically identical to the experimental data at 300 K for both diodes (ignoring the SRH current). Simulations show that this equality is the result of a counterbalance between the lower tunneling probabilities, caused by the larger bandgap, and the increase in internal electric field, caused by the larger Fermi degeneracies and sharper carrier profiles.

The calibrated Urbach energy $E_{0,c/v}$, as shown in Table 3, is somewhat arbitrary, since a good simulation-experiment match is also possible with significantly smaller/larger $E_{0,c/v}$ values (Fig. 7(a)). The calibration results for different Urbach energies have been obtained by recalibrating the $k_{1,c/v}$ parameters, while keeping other parameter values ($E_{1,c/v}$ and $\Delta E_{edge,c/v}$) constant. In fact, our simulations indicate that it is not $E_{0,c/v}$, but the contribution of the extended band-tails DOS closest to $E_{edge,c/v}$, which is actually being calibrated. This can be appreciated from Fig. 7(b), which shows that, for $V_{np} = -0.30$ V and independent of the value of E_0, between 75%-85% of the band-tails current density, $J_{bts,total}$, consists of tunneling transitions involving states of the first 20% of the extended band-tails DOS. This is further illustrated in Fig. 8, where the two dimensional band-tails DOS, $DOS_{2D,bts}$, corresponding to the different values of E_0 in Fig. 7, are displayed. The DOS-values in the shaded area, which represent the first 20% of the extended band-tails, are indeed comparable for all values of E_0. Table 4 then displays the corresponding integrated two dimensional band-tails DOS for different values of $E_{0,c/v}$, whereby the integration is considered over the first 20% of the band-tails DOS, $\rho_{2D,bts,20\%}$. From Table 4, it is clear that $\rho_{2D,bts,20\%}$ changes only slightly as a function of $E_{0,c/v}$ (for $\Delta E_{edge,c/v} = 100$ meV), which is consistent with the result shown in Fig. 7(a). These observations are different from literature which link the Urbach energy to the NDR current swing [15] or conductance swing [14].

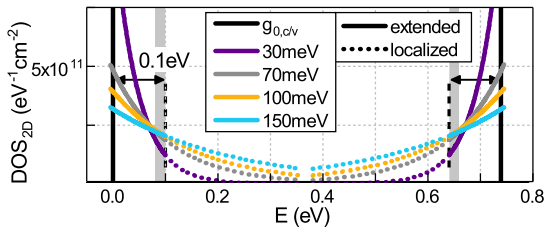

FIGURE 8. The calibrated 2D band-tails DOS for different values of $E_{0,c/v}$. The shaded areas indicate the deepest 20% of the extended part of the band-tails.

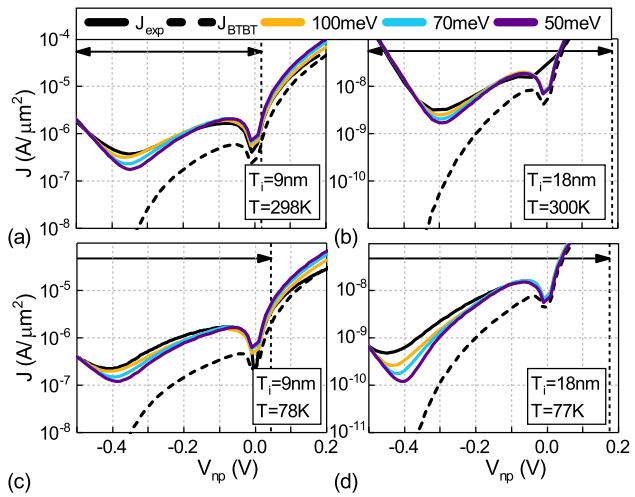

FIGURE 9. Comparison between the calibration results of the band-tails model for different values of $\Delta E_{edge,c/v}$, for the $T_i = 9$ nm Esaki diode at (a) T = 298 K and (c) T = 78 K, and for the $T_i = 18$ nm Esaki diode at (b) T = 300 K and (d) T = 77 K.

Furthermore, a good theory-experiment match can also be obtained for different values of $\Delta E_{edge,c/v}$ (Fig. 9) when the corresponding calibrated parameter set is used (Table 3). However, it is clear that the obtained match becomes worse with smaller values of $\Delta E_{edge,c/v}$. From Table 4, we can see that $\rho_{2D,bts,20\%}$ is inversely proportional to $\Delta E_{edge,c/v}$. The reason being that, if extended states are assumed to exist deeper in the forbidden gap, less states are needed, given the increased tunneling probabilities because of the shorter tunneling paths. Note that the remaining mismatch in Fig. 9 may be an indication that the band-tails DOS is not fully exponential.

VI. IMPACT OF BAND-TAILS ON TFET

In this section, we investigate whether the calibration of Esaki diodes is relevant for TFET performance predictions. In particular, we determine whether the deep tail of extended band-tails states, which is responsible for an observable signature in the NDR current density of the Esaki diodes, is also responsible for an observable signature in the current of TFETs. The TFET which is considered is a homostructure *p-n-i-n* $In_{0.53}Ga_{0.47}As$ TFET with a pocket of 3 nm (Fig. 10(a)). The source and pocket doping level is $5 \times 10^{19}\,cm^{-3}$. For these simulations (Fig. 10(b)-(c)),

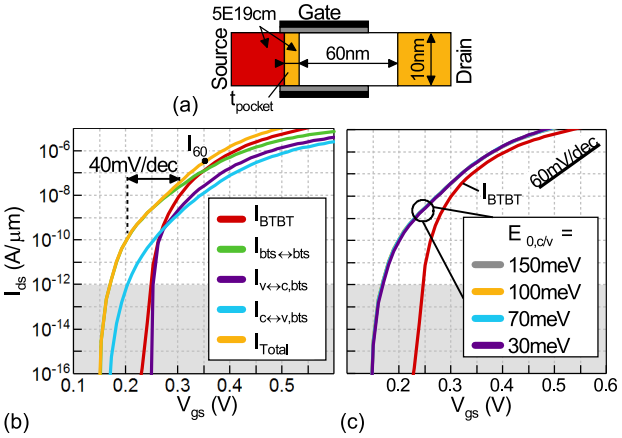

FIGURE 10. (a) Schematic structure of a pocketed *p-n-i-n* $In_{0.53}Ga_{0.47}As$ TFET with $t_{pocket} = 3$ nm and 5×10^{19} cm^{-3} source and pocket doping. (b)-(c) I_{ds}-V_{gs} curves for $V_{ds} = 0.30$ V: (b) The different tunneling contributions of the calibrated band-tails model using the parameter set for $\Delta E_{edge,c/v} = 100$ meV and $E_{0,c/v} = 100$ meV. (c) Comparison of the band-tails model results, I_{Total}, for different values of $E_{0,c/v}$ with $\Delta E_{edge,c/v} = 100$ meV. (b)-(c) Parameter values given by Table 2 (no dopant-dependent BGN) and 3. The shaded area indicates the irrelevant current levels.

a factor of $\sqrt[3]{5/2}$ has been added to $k_{1,c/v}$ to compensate for the $5/2\times$ higher doping concentration in the TFET compared to the $In_{0.53}Ga_{0.47}As$ Esaki diodes of Fig. 1(a).

Fig. 10(b) shows the predicted impact of the different band-tails tunneling contributions on the transfer characteristics of the TFET for $V_{ds} = 0.30$ V. For this simulation, the parameter set for $\Delta E_{edge,c/v} = 100$ meV and $E_{0,c/v} = 100$ meV has been used for the band-tails model. It is observed that the band-tails-to-band-tails tunneling current, $I_{bts\leftrightarrow bts}$, which is directly caused by the band-tails states in the highly-doped pocket and source regions, gives the most significant contribution. This observation is identical to that for the Esaki diodes, where $J_{bts\leftrightarrow bts}$ is also the dominant tunneling current contribution, which means that the tunneling contribution that is relevant for the TFET is indeed being calibrated in the diodes. Note that, because of the long intrinsic channel (60 nm), the band-tails states in the drain have a negligible contribution to the tunneling currents in the on-state.

Next, the impact of the arbitrary value of the Urbach energy, E_0, on the TFET prediction is investigated. Our simulations show that the TFET predictions are also insensitive to the value of $E_{0,c/v}$, provided that the band-tails DOS near $E_{edge,c/v}$ remains about constant (Fig. 10(b)). Similarly to the Esaki diodes, a more detailed investigation shows that, for $V_{gs} = 0.20$ V and independent of the value of E_0, between 67% and 76% of the total band-tails current, $I_{bts,total} = I_{bts\leftrightarrow bts} + I_{v\leftrightarrow c,bts} + I_{c\leftrightarrow v,bts}$, consists of tunneling transitions involving band-tails states of the first 20% of the extended band-tails DOS. This result demonstrates that the same fraction of the extended band-tails DOS determines the dominant band-tails tunneling contribution in both the

NDR regime of the diodes and the subthreshold region of the TFET, which proves that the calibration of Esaki diodes is relevant for TFETs. Furthermore, we conclude that, like the current swing in the NDR regime of an Esaki diode, the SS of a TFET device is not determined by the Urbach energy of the high-doping-induced band-tails.

The impact of the ballistic band-tails tunneling contributions on the transfer characteristics of the TFET manifests itself mainly in two ways. The first way is through a shift of the onset voltage, which is the voltage for which a relevant tunneling current ($I_{ds} \geqslant 1\,pA\,\mu m^{-1}$) is observed, to a smaller V_{gs} (from 0.25 V to about 0.15 V). The reason for this shift is that, because the band-tails extend into the bandgap, ballistic tunneling transitions involving band-tails states can occur at smaller V_{gs} than conventional BTBT transitions. The second way in which the impact of band-tails becomes noticeable is through the decrease of the I_{on}/I_{off}-ratio for a given supply voltage window. This decrease is the result of the increase of the average SS of the total current, I_{total}, when compared to the average SS of the BTBT current, I_{BTBT}. However, though the average SS is increased when one accounts for band-tails tunneling, the I_{60} is barely affected and remains around $0.5\,\mu A\,\mu m^{-1}$ (Fig. 10(b)).

Note that band-tails might also impact the temperature dependence of the transfer characteristics and the subthreshold swing of TFET devices based on an interplay of the three phenomena listed for the Esaki diodes. A detailed study of this temperature dependence is beyond the scope of this work, which focuses on resolving the theory-experiment discrepancy.

VII. BAND-TAILS IN INAS ESAKI DIODES

Lastly, we demonstrate that the described procedure for band-tails calibration can be applied to all direct-bandgap semiconductor materials. This is done based on the measured current-voltage characteristics of two highly-doped InAs Esaki diodes. The devices under consideration have been fabricated and measured by Pawlik *et al.* as reported in [19]. The Esaki diodes have a *p-i-n* structure where the intrinsic region thickness has a target value of 3 nm. Contrary to the $In_{0.53}Ga_{0.47}As$ Esaki diodes, the InAs diodes have different doping profiles. The *n*-type silicon doping concentration for the first Esaki diode ('InAs-1') is $N_D = 3 \times 10^{18}\,cm^{-3}$, whereas it is $N_D = 1 \times 10^{19}\,cm^{-3}$ for the second diode ('InAs-2'). For both diodes, the *p*-type beryllium doping concentration is $N_A = 1.8 \times 10^{19}\,cm^{-3}$. Aside from SIMS-based average doping concentrations [37], no doping profiles, allowing to extract information about the junction profiles, or C-V characteristics are available, which increases the error bar on the BTBT and band-tails calibration.

The result of the calibration is shown in Fig. 11 for both InAs Esaki diodes. Note that the measured I_{ds}-V_{ds} curves have been corrected for series resistance such that an appropriate slope for the diffusion current is obtained (the current density in the NDR regime of both diodes is unaffected by this correction). For the calibration, $\Delta E_{edge,c/v} = 70\,meV$ and $E_{0,c/v} = 100\,meV$ are assumed for the band-tails model. From Fig. 11, it is clear that a good match can be obtained in both the reverse- and forward-bias regime of the Esaki diodes, when the band-tails tunneling contributions are taken into account. In addition, our simulations indicate that the band-tails DOS increases with the doping concentration, which is an expected dependence [27]. More specifically, the predicted band-tails DOS of the more highly-doped 'InAs-2' diode is 6× larger than the predicted band-tails DOS in the 'InAs-1' diode, which is in agreement with the 3× higher *n*-type doping concentration in the former. However, a more extensive study is necessary to fully understand the relationship between the doping concentration and the resulting density of band-tails states. Overall, the achieved match and the meaningful interpretation of the obtained results further support and validate the hypothesis that the current density in the NDR regime is a signature of ballistic band-tails tunneling.

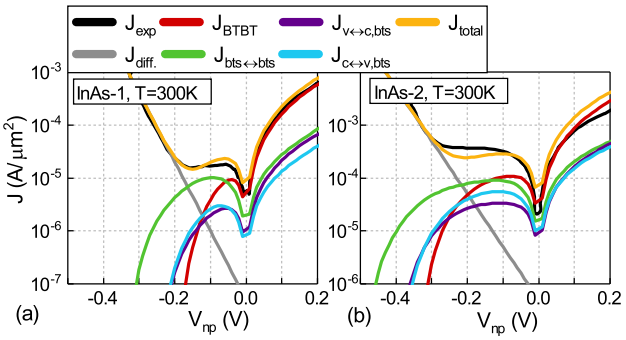

FIGURE 11. Comparison between the measured and simulated (using the band-tails model) current-voltage characteristics for the (a) 'InAs-1' and (b) 'InAs-2' *p-i-n* Esaki diodes at T = 300 K. $J_{diff.}$ is an exponential fit to the SRH current.

VIII. CONCLUSION

In conclusion, ballistic band-tails tunneling contributions can fully resolve the simulation-experiment discrepancy in the NDR regime of highly-doped Esaki diodes, based on direct-bandgap semiconductor materials. In particular, using a SC model for high-doping-induced band-tails current, the reverse- and forward-bias current-voltage characteristics of two $In_{0.53}Ga_{0.47}As$ Esaki diodes with identical *n*- and *p*-type doping profiles have been matched at two temperatures while correlating the band-tails DOS to the doping level. In addition, we have demonstrated that the procedure can be used to extract quantitative values for the band-tails DOS from I-V measurements. When applied to InAs Esaki diodes, our procedure predicts, as expected, a higher band-tails DOS for the more highly-doped diode. Furthermore, we find that the calibration of Esaki diodes is relevant for TFET predictions. Lastly, we observe that the current swing in the NDR regime of an Esaki diode and the SS of a *p-n-i-n* TFET are not determined by the Urbach energy, but rather by the density of extended band-tails states in a small ($\leqslant 20\,meV$) energy range which is deepest in the bandgap. These insights will

improve future predictive work for BTBT-based currents in TFET and MOSFET.

ACKNOWLEDGMENT

J. Bizindavyi gratefully acknowledges FWO-Vlaanderen for a Strategic Basic Research PhD fellowship.

REFERENCES

[1] U. E. Avci, D. H. Morris, and I. A. Young, "Tunnel field-effect transistors: Prospects and challenges," *IEEE J. Electron Devices Soc.*, vol. 3, no. 3, pp. 88–95, May 2015.

[2] D. Cavalheiro, F. Moll, and S. Valtchev, "Prospects of tunnel FETs in the design of power management circuits for weak energy harvesting DC sources," *IEEE J. Electron Devices Soc.*, vol. 6, pp. 382–391, May 2018.

[3] D. Verreck, G. Groeseneken, and A. Verhulst, "The tunnel field-effect transistor," in *Wiley Encyclopedia of Electrical and Electronics Engineering*. Hoboken, NJ, USA: Wiley, Sep. 2016, pp. 1–24.

[4] E. Lind, E. Memiševič, A. W. Dey, and L.-E. Wernersson, "III-V heterostructure nanowire tunnel FETs," *IEEE J. Electron Devices Soc.*, vol. 3, no. 3, pp. 96–102, May 2015.

[5] H. Lu and A. Seabaugh, "Tunnel field-effect transistors: State-of-the-art," *IEEE J. Electron Devices Soc.*, vol. 2, no. 4, pp. 44–49, Jul. 2014.

[6] A. M. Ionescu and H. Riel, "Tunnel field-effect transistors as energy-efficient electronic switches," *Nature*, vol. 479, no. 7373, pp. 329–337, Nov. 2011.

[7] S. Sant *et al.*, "Lateral InAs/Si P-type tunnel FETs integrated on Si—Part 2: Simulation study of the impact of interface traps," *IEEE Trans. Electron Devices*, vol. 63, no. 11, pp. 4240–4247, Nov. 2016.

[8] M. Mohammed *et al.*, "Electric-field induced quantum broadening of the characteristic energy level of traps in semiconductors and oxides," *J. Appl. Phys.*, vol. 120, no. 24, Dec. 2016, Art. no. 245704.

[9] J. Charles *et al.*, "Incoherent transport in NEMO5: Realistic and efficient scattering on phonons," *J. Comput. Electron.*, vol. 15, no. 4, pp. 1123–1129, Dec. 2016.

[10] J. T. Teherani *et al.*, "Auger generation as an intrinsic limit to tunneling field-effect transistor performance," *J. Appl. Phys.*, vol. 120, no. 8, Aug. 2016.

[11] S. Sant and A. Schenk, "The effect of density-of-state tails on band-to-band tunneling: Theory and application to tunnel field effect transistors," *J. Appl. Phys.*, vol. 122, no. 13, Oct. 2017, Art. no. 135702.

[12] M. A. Khayer and R. K. Lake, "Effects of band-tails on the subthreshold characteristics of nanowire band-to-band tunneling transistors," *J. Appl. Phys.*, vol. 110, no. 7, 2011, Art. no. 074508.

[13] H. Zhang, W. Cao, J. Kang, and K. Banerjee, "Effect of band-tails on the subthreshold performance of 2D tunnel-FETs," in *Proc. IEEE Int. Electron Devices Meeting (IEDM)*, San Francisco, CA, USA, Dec. 2016, pp. 30.3.1–30.3.4.

[14] S. Agarwal and E. Yablonovitch, "Band-edge steepness obtained from Esaki/backward diode current-voltage characteristics," *IEEE Trans. Electron Devices*, vol. 61, no. 5, pp. 1488–1493, May 2014.

[15] E. Memisevic, E. Lind, M. Hellenbrand, J. Svensson, and L.-E. Wernersson, "Impact of band-tails on the subthreshold swing of III-V tunnel field-effect transistor," *IEEE Electron Device Lett.*, vol. 38, no. 12, pp. 1661–1664, Dec. 2017.

[16] J. I. Pankove, "Absorption edge of impure gallium arsenide," *Phys. Rev.*, vol. 140, no. 6A, pp. A 2059–A 2065, Dec. 1965.

[17] A. K. Kalkan, S. J. Fonash, and S.-C. Cheng, "Band-tail photoluminescence in nanocrystalline Si," *Appl. Phys. Lett.*, vol. 77, no. 1, pp. 55–57, Jul. 2000.

[18] H. Kato, N. Kashio, Y. Ohki, K. S. Seol, and T. Noma, "Band-tail photoluminescence in hydrogenated amorphous silicon oxynitride and silicon nitride films," *J. Appl. Phys.*, vol. 93, no. 1, pp. 239–244, Jan. 2003.

[19] D. Pawlik *et al.*, "Benchmarking and improving III-V Esaki diode performance with a record 2.2 MA/cm2 peak current density to enhance TFET drive current," in *Proc. Int. Electron Devices Meeting*, Dec. 2012, pp. 27.1.1–27.1.3.

[20] Q. Smets *et al.*, "InGaAs tunnel diodes for the calibration of semi-classical and quantum mechanical band-to-band tunneling models," *J. Appl. Phys.*, vol. 115, no. 18, May 2014, Art. no. 184503.

[21] *Sentaurus Device User Guide, Version N-2017.09*, Synopsys, Mountain View, CA, USA, 2017.

[22] J. Bizindavyi, "Calibration of parasitic effects in tunnel field-effect transistors," M.S. thesis, Faculty Eng. Sci., KU Leuven, Leuven, Belgium, 2016.

[23] S. Jain and D. Roulston, "A simple expression for band gap narrowing (BGN) in heavily doped Si, Ge, GaAs and GeSi strained layers," *Solid State Electron.*, vol. 34, no. 5, pp. 453–465, May 1991.

[24] S. C. Jain, R. P. Mertens, and R. J. Van Overstraeten, "Bandgap narrowing and its effects on the properties of moderately and heavily doped germanium and silicon," *Adv. Electron. Electron Phys.*, vol. 82, pp. 197–275, 1991.

[25] W.-S. Cho *et al.*, "Full band atomistic modeling of homo-junction InGaAs band-to-band tunneling diodes including band gap narrowing," *Appl. Phys. Lett.*, vol. 100, no. 6, Feb. 2012, Art. no. 063504.

[26] Q. Smets *et al.*, "Calibration of bulk trap-assisted tunneling and Shockley-read-hall currents and impact on InGaAs tunnel-FETs," *IEEE Trans. Electron Devices*, vol. 64, no. 9, pp. 3622–3626, Sep. 2017.

[27] P. Van Mieghem, "Theory of band tails in heavily doped semiconductors," *Rev. Mod. Phys.*, vol. 64, no. 3, pp. 755–793, Jul. 1992.

[28] J. Bizindavyi *et al.*, "Calibration of the high-doping induced ballistic band-tails tunneling current with In0.53Ga0.47As Esaki diodes," in *Proc. 5th Berkeley Symp. Energy Efficient Electron. Syst. Steep Transistors Workshop (E3S)*, Berkeley, CA, USA, Oct. 2017, pp. 1–3.

[29] J. Serre, A. Ghazali, and P. L. Hugon, "Band tailing in heavily doped semiconductors. Scattering and impurity-concentration-fluctuation effects," *Phys. Rev. B, Condens. Matter*, vol. 23, no. 4, pp. 1971–1976, 1981.

[30] J. Dong and D. A. Drabold, "Band-tail states and the localized-to-extended transition in amorphous diamond," *Phys. Rev. B, Condens. Matter*, vol. 54, no. 15, pp. 10284–10287, Oct. 1996.

[31] D. A. Drabold and J. Dong, "Band tail states and the Anderson transition in amorphous silicon," *J. Non Cryst. Solids*, vols. 227–230, pp. 153–157, May 1998.

[32] R. Tsu and L. Esaki, "Tunneling in a finite superlattice," *Appl. Phys. Lett.*, vol. 22, no. 11, pp. 562–564, Jun. 1973.

[33] D. Verreck, "Quantum mechanical transport towards the optimization of heterostructure tunnel field-effect transistors," Ph.D. dissertation, Faculty Eng. Sci., KU Leuven, Leuven, Belgium, 2017.

[34] A. S. Verhulst *et al.*, "Inherent transmission probability limit between valence-band and conduction-band states and calibration of tunnel-FET parasitics," in *Proc. 5th Berkeley Symp. Energy Efficient Electron. Syst. Steep Transistors Workshop (E3S)*, Berkeley, CA, USA, Oct. 2017, pp. 1–3.

[35] E. O. Kane, "Thomas–Fermi approach to impure semiconductor band structure," *Phys. Rev.*, vol. 131, no. 1, pp. 79–88, Jul. 1963.

[36] E. O. Kane, "Band tails in semiconductors," *Solid State Electron.*, vol. 28, nos. 1–2, pp. 3–10, Jan. 1985.

[37] D. J. Pawlik, "Comprehensive mapping and benchmarking of Esaki diode performance," Ph.D. dissertation, Rochester Inst. Technol., New York, NY, USA, 2013.

JASPER BIZINDAVYI received the B.Sc. degree in engineering science and the M.Sc. degree in nanoscience, nanotechnology and nanoengineering from KU Leuven, Leuven, Belgium, in 2014 and 2016, respectively.

He is currently pursuing the Ph.D. degree with KU Leuven, where his research focuses on the modeling of parasitic effects in tunnel field-effect transistors.

ANNE S. VERHULST received the Ph.D. degree in electrical engineering from Stanford University, Stanford, CA, USA, in 2004. She joined imec, Leuven, Belgium, in 2005.

Her research interests include modeling, calibration, and fabrication of tunnel field-effect transistors.

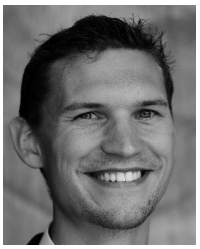

QUENTIN SMETS received the Erasmus Mundus Master degree in nanoscience and nanotechnology jointly from KU Leuven, Belgium, and the Chalmers University of Technology, Gothenburg, Sweden, in 2010 and the Ph.D. degree from KU Leuven in 2016, focusing on III-V TFETs at imec, Belgium.

He is currently a Researcher with imec. His interests include MOSFETs and TFETs with 2-D materials.

DEVIN VERRECK received the M.S. degree in nanoscience and nanotechnology and the Ph.D. degree in electrical engineering from KU Leuven, Leuven, Belgium, in 2012 and 2017, respectively.

He is currently with imec, Belgium, where his research focuses on the modeling of advanced semiconductor devices.

BART SORÉE (M'08) received the M.Sc. degree in civil engineering physics and the M.Sc. degree in theoretical physics from Universiteit Gent, Ghent, Belgium, in 1998 and 1999, respectively, and the Ph.D. degree from KU Leuven, Leuven, Belgium, in 2003. In 2014, he joined imec, where he is currently a Principal Scientist with the Physics, Modeling and Simulation Group. He also joined the Condensed Matter Theory Group, Physics Department, Universiteit Antwerpen, Antwerp, Belgium, in 2011 and the Department of Electrical Engineering with KU Leuven, in 2014.

His research interests include quantum transport, physics and modeling of devices, nonequilibrium statistical mechanics, and identifying novel and emerging device concepts and materials. He is a member of the American Physical Society.

GUIDO GROESENEKEN (S'80–M'89–SM'95–F'05) received the M.Sc. degree in electrical and mechanical engineering and the Ph.D. degree in applied sciences from KU Leuven, Leuven, Belgium, in 1980 and 1986, respectively. In 1987, he joined the Research and Development Laboratory, imec, where he is responsible for research in reliability physics for deep submicrometer CMOS technologies. He has been a Professor with KU Leuven since 2001, where he is responsible for coordinating the Erasmus Mundus Master Program in nanoscience and nanotechnology.

His research interests include the electrical characterization and reliability of novel CMOS and Beyond CMOS devices. He has authored or co-authored over 300 publications in international scientific journals and in international conference proceedings and seven book chapters. He is the holder of ten patents in his fields of expertise. He was a recipient of the IEEE Cledo Brunetti Award in 2017. He became a imec fellow in 2007.